Reno, Nevada
NOISE-CON 2007
2007 October 22-24

Improved gear whine model with focus on friction-induced structure-borne noise

Song He[a]
Rajendra Singh[b]
The Ohio State University
201 West 19th Ave.
Columbus, OH 43210

Goran Pavic[c]
INSA de Lyon
25 bis avenue Jean Capelle
69621 Villeurbanne, France

ABSTRACT

An improved source-path-receiver model is developed and validated to quantify the effect of sliding friction on structure-borne gear whine noise. By assuming rigid bearings due to impedance mismatch, the source sub-system of a spur gear pair predicts interfacial bearing forces in the line-of-action and off line-of-action directions for two whine excitations (static transmission error and sliding friction). Next, a finite-element gearbox model with embedded bearing stiffness matrices is developed to characterize structural paths for the calculation of surface velocity distributions. Predictions are validated by comparing with transfer function measurements from gear mesh to the housing plates. Radiated noise is then estimated by using two methods, namely the Rayleigh integral method and a substitute source technique. Approximations are validated by comparing calculations with measured noise data under running experiments. Proposed model provides an efficient tool to quantify the relative contribution of sliding friction to the structure-borne noise, which is found to be significant when the transmission error is minimized.

1. INTRODUCTION

Gears are known to be one of the major vibro-acoustic sources in many practical systems including ground and air vehicles such as heavy-duty trucks and helicopters. Typically, steady state gear (whine) noise is generated by several sources and the reduction of gear noise is often challenging for most products. Virtually all prior researchers[1-3] have assumed the main exciter to be the static transmission error (STE) that is defined as the derivation from the ideal tooth profile induced by manufacturing errors and elastic deformations. However, high precision gears are still unacceptably noisy in practice. When the transmission error has been minimized (say via modifying the tooth profile), the sliding friction remains as a potential contributor to gear noise and vibration. Further, most prior research on gear friction[4-6] has been confined to the dynamic analysis of the gear pair source sub-system and no attempt has been made to examine the friction related structural path and noise radiation issues. To fill in this void, the main objectives of this

[a] Email address: he.81@osu.edu
[b] Email address: singh.3@osu.edu
[c] Email address: goran.pavic@insa-lyon.fr

research are thus to: First, propose a refined source-path-receiver model that characterizes the structural paths in two directions and, second, propose analytical tools to efficiently predict the whine noise and quantify the contribution of sliding friction to the overall whine noise. The system model is depicted in Fig. 1. The source sub-system includes the spur gear pair and shafts inside the gearbox; these are characterized by a 6 degree-of-freedom (DOF) linear-time-varying model[6]. The transmission error dominated bearing forces in the line-of-action (LOA) direction and friction dictated bearing forces in the off line-of-action (OLOA) direction are coupled and transmitted to the housing structure. Radiated sound pressure $p(\omega)$ from gearbox panels (at gear mesh frequencies) are then received by microphone(s). Analytical predictions of the structural transfer function and noise radiation will be compared with measurements.

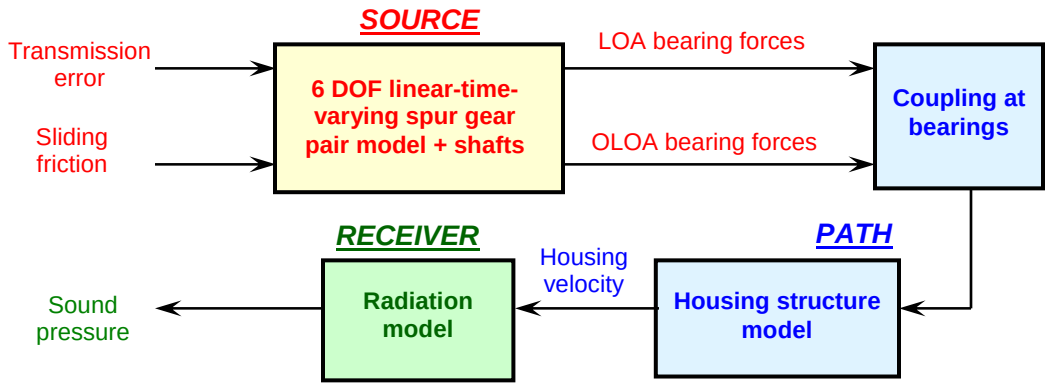

Figure 1: Block diagram for the vibro-acoustics of a simplified geared system with two excitations at the gear mesh.

2. SOURCE SUB-SYSTEM MODEL

The source sub-system is described by a recently developed[6] 6DOF, linear time-varying spur gear pair model that incorporates the sliding friction and realistic mesh stiffness, which is calculated by an accurate finite element/contact mechanical code[7]. Rigid bearing is assumed as boundary conditions due to the impedance mismatch at the shaft/bearing interface. Overall, the system formulations are summarized as following. The governing equations for the torsional motions $\theta_p(t)$ and $\theta_g(t)$ of pinion and gear are:

$$J_p\ddot{\theta}_p(t) = T_p + \sum_{i=0}^{n} X_{pi}(t)F_{pfi}(t) - \sum_{i=0}^{n} r_{bp}N_{pi}(t), \quad J_g\ddot{\theta}_g(t) = -T_g + \sum_{i=0}^{n} X_{gi}(t)F_{gfi}(t) + \sum_{i=0}^{n} r_{bg}N_{gi}(t) \quad (1,2)$$

where n = floor(σ) in which the "floor" function rounds off the contact ratio σ to the nearest integer (towards a lower value); J_p and J_g are the polar moments of inertia of the pinion and gear; T_p and T_g are the external and braking torques; r_{bp} and r_{bg} are base radii of the pinion and gear; and, $N_{pi}(t)$ and $N_{gi}(t)$ are the normal loads defined as follows:

$$\begin{aligned} N_{pi}(t) = N_{gi}(t) = k_i(t)\left[r_{bp}\theta_p(t) - r_{bg}\theta_g(t) + x_p(t) - x_g(t)\right] \\ + c_i(t)\left[r_{bp}\dot{\theta}_p(t) - r_{bg}\dot{\theta}_g(t) + \dot{x}_p(t) - \dot{x}_g(t)\right] \end{aligned} \quad (3)$$

where $k_i(t)$ and $c_i(t)$ are the realistic mesh stiffness and viscous damping profiles; $x_p(t)$ and $x_g(t)$ denote the LOA displacements of pinion and gear centers. The sliding friction forces $F_{pfi}(t)$ and $F_{gfi}(t)$ as well as their moment arms $X_{pi}(t)$ and $X_{gi}(t)$ of the i^{th} meshing pair are derived as:

$$F_{pfi}(t) = \mu_i(t)N_{pi}(t), \qquad F_{gfi}(t) = \mu_i(t)N_{gi}(t) \quad (4a,b)$$

$$X_{pi}(t) = L_{XA} + (n-i)\lambda + \mathrm{mod}(\Omega_p r_{bp}t, \lambda), \quad X_{gi}(t) = L_{YC} + i\lambda - \mathrm{mod}(\Omega_g r_{bg}t, \lambda) \quad (5a,b)$$

where the sliding friction is formulated by $\mu_i(t) = \mu_0 \,\mathrm{sgn}\left[\mathrm{mod}(\Omega_p r_{bp} t, \lambda) + (n-i)\lambda - L_{AP}\right]$; λ is the base pitch; "sgn" is the sign function; the modulus function mod(x, y) = $x - y$ ·floor(x/y), if y≠0; Ω_p and Ω_g are the nominal speeds (in rad/s); and, L_{AP}, L_{XA} and L_{YC} are geometric length constants[6]. The governing equations for $x_p(t)$ and $x_g(t)$ motions in the LOA direction are:

$$m_p \ddot{x}_p(t) + 2\zeta_{pSx}\sqrt{K_{pSx} m_p}\,\dot{x}_p(t) + K_{pSx} x_p(t) + \sum_{i=0}^{n} N_{pi}(t) = 0 \tag{6}$$

$$m_g \ddot{x}_g(t) + 2\zeta_{gSx}\sqrt{K_{gSx} m_g}\,\dot{x}_g(t) + K_{gSx} x_g(t) + \sum_{i=0}^{n} N_{gi}(t) = 0 \tag{7}$$

Here, m_p and m_g are the masses of the pinion and gear; K_{pSx} and K_{gSx} are the effective shaft stiffness values in the LOA direction, and ζ_{pSx} and ζ_{gSx} are the damping ratios. Likewise, the translational motions $y_p(t)$ and $y_g(t)$ in the OLOA direction are governed by:

$$m_p \ddot{y}_p(t) + 2\zeta_{pSy}\sqrt{K_{pSy} m_p}\,\dot{y}_p(t) + K_{pSy} y_p(t) - \sum_{i=0}^{n} F_{pfi}(t) = 0 \tag{8}$$

$$m_g \ddot{y}_g(t) + 2\zeta_{gSy}\sqrt{K_{gSy} m_g}\,\dot{y}_g(t) + K_{gSy} y_g(t) - \sum_{i=0}^{n} F_{gfi}(t) = 0 \tag{9}$$

Both LOA and OLOA bearing forces are predicted for the example case (unity-ratio NASA spur gear pair whose parameters are listed in Table 1) and compared in Fig. 2 at the first three gear mesh frequencies as a function of pinion torque T_p. Observe that the friction dominated OLOA dynamic responses are less sensitive to a variation in T_p.

Table 1: Parameters of the example case: NASA spur gear pair with unity ratio (with long tip relief)

Parameter/property	Pinion/Gear	Parameter/property	Pinion/Gear
Number of teeth	28	Face width, in	0.25
Diametral pitch, in^{-1}	8	Tooth thickness, in	0.191
Pressure angle, º	20	Center distance, in	3.5
Outside diameter, in	3.738	Elastic modulus, psi	30×10^6
Root diameter, in	3.139	Shaft stiffness, lb/in	1.29×10^5

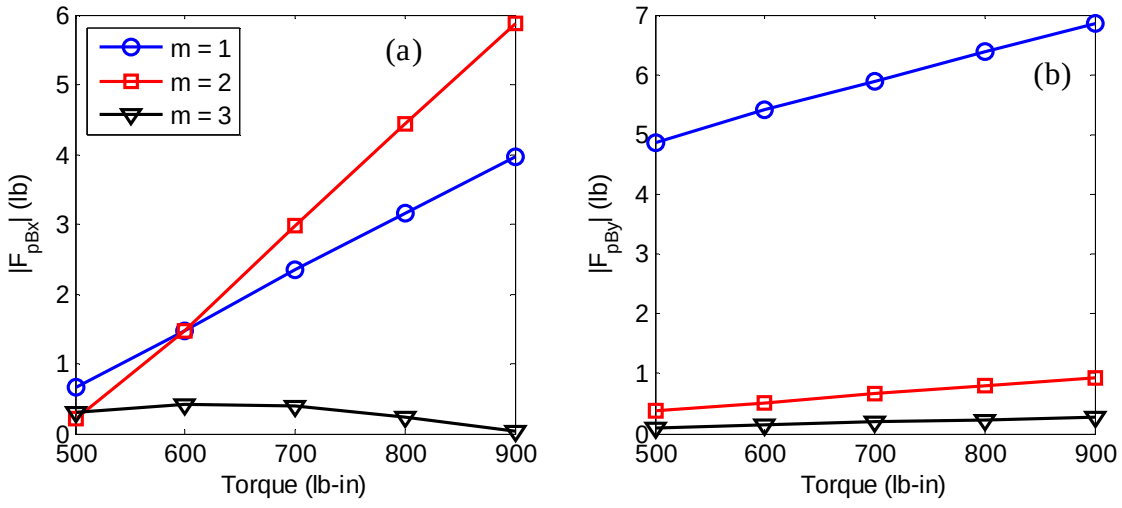

Figure 2: Bearing forces predicted under varying T_p given Ω_p = 4875 RPM and 140 °F. (a): LOA bearing force; (b) OLOA bearing force. Key: m is the mesh frequency index. (Note: These predictions have been validated by experiments[6])

3. STRUCTRUAL PATH WITH FRICTION CONTRIBUTION

A. Bearing and housing models

Predicted bearing forces by the source sub-system provide excitations to the multi-input multi-output (MIMO) structural paths for the gearbox of Fig. 3(a). Force excitations are coupled at each bearing via a 6 by 6 stiffness matrix $[K]_{Bm}$ which is calculated by using the algorithm proposed by Lim and Singh[8]. Nominal shaft loads and bearing preloads are assumed to ensure a time-invariant $[K]_{Bm}$. In order to focus on the transmission error path and frictional path in the LOA and OLOA directions respectively, $[K]_{Bm}$ is further simplified into a 2 by 2 matrix by neglecting the moment transfer[9] and assuming that no axial force is generated by the spur gear sub-system. Calculated nominal bearing stiffness[8] are $K_{Bx} = K_{By} = 2.8\times10^6$ lb/in at mean operating conditions; these are much larger than the shaft stiffness of 1.29×10^5 lb/in. This is consistent with the impedance mismatch assumption made at the shaft/bearing interface.

The implementation of $[K]_{Bm}$ into the finite element gearbox model of Fig. 3(b) is given special attention[10-11]. At high mesh frequencies (say up to 5 kHz), the dimensions of the bearings are comparable to the plate flexural wavelength. Hence the holes may significantly alter the plate dynamics and such effects must be modeled[11]. A rigid (with Young's modulus 100 times higher than the casing steel) and mass-less (with density 1% of the casing steel) beam element is used to model the interface from shaft to bearing. Its length is chosen to be very short to avoid the introduction of any beam resonances in the frequency range of interest. The shaft beam element is connected to the central bearing node though orthogonal foundation stiffness (K_{Bx} and K_{By}) in the LOA and OLOA directions, respectively. The central node is then connected to the circumferential bearing nodes by 12 rigid and mass-less beams (one at each rolling element's angular position) which form a star configuration, such that the displacement of the plate around the bearing hole are equal to the "housing node" at the center.

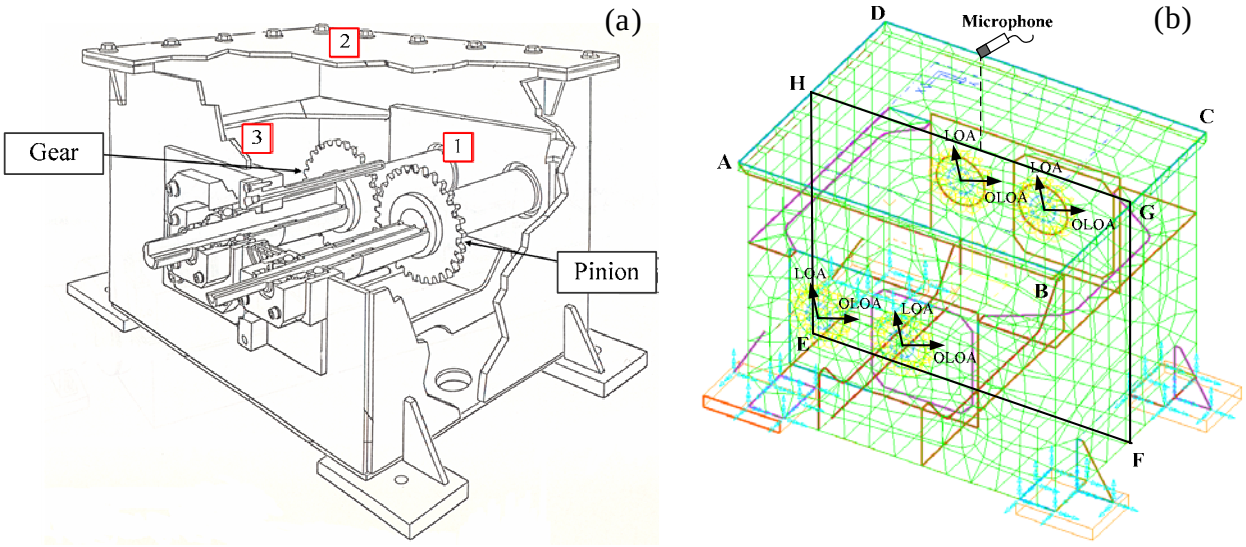

Figure 3: (a) Schematic of NASA gearbox; (b) Finite element model of NASA gearbox with embedded bearing stiffness matrices.

B. Experimental studies and validation of structural model

The finite element model of Fig. 3(b) is created by using I-DEAS for the NASA gearbox with bearing holes, embedded stiffness matrices $[K]_{Bm}$, stiffening plates as well as clamped boundary conditions at four rigid mounts. Although the gear pair and shafts are not included, it

has been shown[8,10] that an "empty" gearbox tends to describe the dynamics of the entire gearbox system. Table 2 confirms that the natural frequencies predicted by the finite element model correlate well with measurements reported by Oswald et al.[12] despite minor modifications made to the gearbox. Mode shape predictions also match well with modal tests, and Fig. 4 gives a typical comparison of structural mode at the 8th natural frequency (f_n = 2962 Hz).

Table 2: Comparison of measured natural frequencies[12] and finite element predictions

Method/mode index	1	2	3	4	5	6	7	8
Measurements[7] (Hz)	658	1049	1709	2000	2276	2536	2722	2962
Finite element predictions (Hz)	650	988	1859	1940	2328	2566	2762	2962

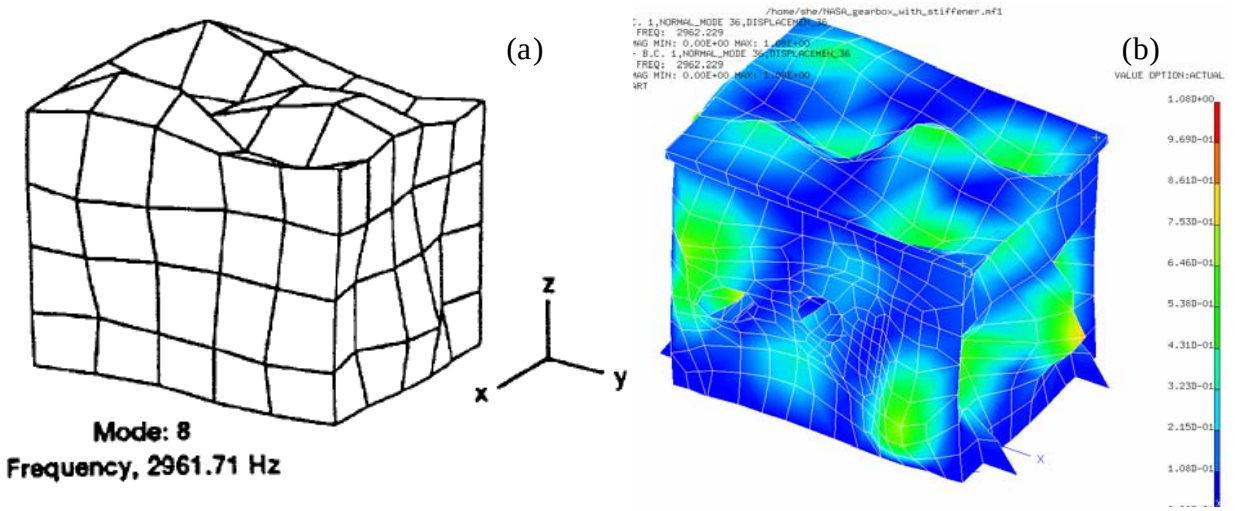

Figure 4: Comparison of the gearbox mode shape at 2962 Hz: (a) modal experiment result[12]; (b) finite element prediction.

In order to validate the structural paths, several transfer functions were measured for the NASA gearbox by assuming that the quasi-static system response is similar to the response under non-resonant rotating conditions. The gearbox was modified to allow controlled excitations to be applied to the gear-mesh and measured. Brackets were welded to the bedplate of the gear-rig to mount shakers in the LOA and OLOA directions outside the gearbox, as shown in Fig. 5(a). Stinger rods were connected from the shakers through two small holes in the gearbox and attached to a collar on the input shaft. Two mini accelerometers were fastened to a block behind the loaded gear tooth to measure the LOA and OLOA mesh accelerations. Band-limited random noise signals were then used as excitation signals and tests were done with only one shaker activated at a time with a 600 lb-in static preload. Dynamic responses were measured to generate vibro-acoustic transfer functions. Sensor # 1 of Fig. 3(a) is a tri-axial accelerometer mounted on the output shaft bearing cap to measure the LOA, OLOA, and axial vibrations. Sensors #2 and #3 are unidirectional accelerometers mounted on the top and back plates, respectively.

The transfer function of the combined source-path sub-systems is predicted as following:

$$\tilde{H}_{S-P}(\omega) = \tilde{H}_S(\omega) \cdot \tilde{H}_P(\omega) = \tilde{H}_S(\omega) \cdot \frac{\tilde{Y}_{plate}(\omega)}{\tilde{Y}_{bearing}(\omega)} \tag{10}$$

where $\tilde{H}_S(\omega)$ is the motion transmissibility from mesh excitation to translational bearing responses (in LOA or OLOA directions) by using a 6DOF linear time-invariant spur gear model[13]. Note that such a lumped model is insufficient to capture the bending and flexural modes

of the gear flanks and shafts. Here, $\tilde{Y}_{plate}(\omega)$ and $\tilde{Y}_{bearing}(\omega)$ are the transfer and driving point mobilities for the (top) plate and the bearing; these are derived from the finite element gearbox model by using the modal expansion method with 1% structural damping for all modes. Figure 5(b) shows that the predicted motion transmissibility from gear mesh to the top plate correlates reasonably well with measurement given the complexity of the geared system. The highest frequency is chosen such that the shortest wave-length is 4 times larger than the mesh dimension on the top plate. Recall that the interactions between the shaft and bearings/casing were neglected in our model by the impedance mismatch assumption. Consequently, a 10 dB empirical (but uniformly applied) weighting function w is used to "tune" the magnitude of transfer mobility prediction in Fig. 5(b) for a better comparison.

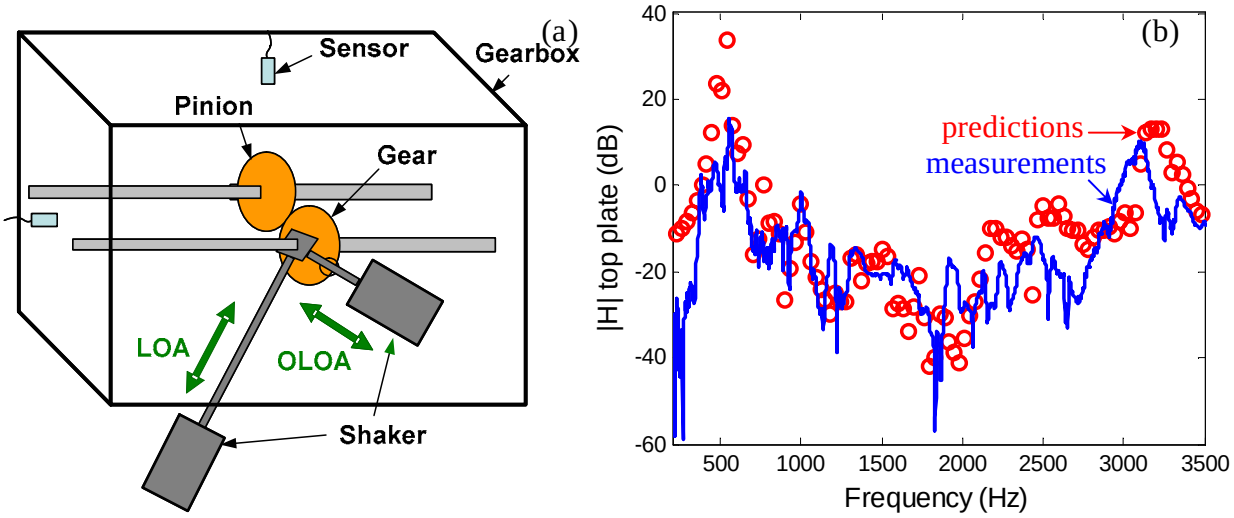

Figure 5: (a) Experiment used to measure structural transfer functions; (b) Comparison of transfer function magnitudes from gear mesh to the sensor on top plate. Key: ——, measurements; ○, predictions.

C. Comparison of structural paths in LOA and OLOA directions

First, assume that (i) the bearing forces predicted by the lumped source model[6] are in phase at either bearing end for both the pinion and gear shafts; and (ii) the bearing forces of pinion and gear are same in magnitude but opposite in directions due to the symmetry of unity ratio gear pair. Second, the overall structural paths are derived for the transmission error controlled LOA (or x) path and the friction dominated OLOA (or y) path in terms of combined effective transfer mobilities $\tilde{Y}_{e,x}(\omega)$ and $\tilde{Y}_{e,y}(\omega)$:

$$\tilde{Y}_{e,x}(\omega) = \sum_n w_{p,x,n}\tilde{Y}_{p,x,n}(\omega) - \sum_n w_{g,x,n}\tilde{Y}_{g,x,n}(\omega) \tag{11a}$$

$$\tilde{Y}_{e,y}(\omega) = \sum_n w_{p,y,n}\tilde{Y}_{p,y,n}(\omega) - \sum_n w_{g,y,n}\tilde{Y}_{g,y,n}(\omega) \tag{11b}$$

where w is the empirical weighting function (10 dB, as discussed in the previous section); and the subscript n is the index of the two ends of pinion/gear shafts. Figure 6 compares the magnitudes of $\tilde{Y}_{e,x}(\omega)$ and $\tilde{Y}_{e,y}(\omega)$ at the sensor location on the top plate. Different peaks are observed in the LOA and OLOA paths spectra. This implies that at certain frequencies (e.g. 650 and 1700 Hz), the OLOA path (and thus the frictional effects) could be dominant over the LOA path (and thus the transmission error effects) given comparable force excitation levels. The proposed method thus provides a design tool to quantify and evaluate the relative contribution of

structural path due to sliding friction. The top plate velocity distribution $\tilde{V}_{top}(\omega)$ could then be predicted by using Eq. (12), where $\tilde{F}_{p,B,x}(\omega)$ and $\tilde{F}_{p,B,y}(\omega)$ are the pinion bearing forces predicted by the lumped source model in the LOA and OLOA directions. Figure 7(a) shows the surface interpolated velocity distributions on the top plate at three mesh harmonics (m =1, 2, 3) given T_p = 500 lb-in and Ω_p = 4875 RPM.

$$\tilde{V}_{top}(\omega) = \frac{1}{2}\tilde{F}_{p,B,x}(\omega)\tilde{Y}_{e,x}(\omega) + \frac{1}{2}\tilde{F}_{p,B,y}(\omega)\tilde{Y}_{e,y}(\omega) \tag{12}$$

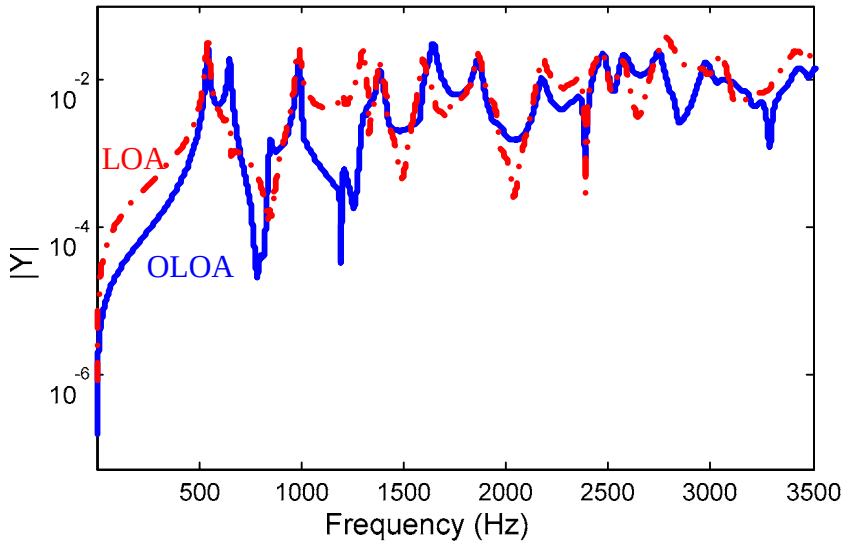

Figure 6: Magnitudes of the combined transfer mobilities in two directions calculated at the sensor location on the top plate. Key: ——, mobility of the OLOA path; – · – · –, mobility of the LOA path.

4. PREDICTION OF NOISE RADIATION AND CONTRIBUTION OF FRICTION

A. Prediction using Rayleigh integral technique

Since the rectangular top plate is the main radiator[14] of the gearbox due to its relatively high mobility, Rayleigh integral[15] is used to approximate the sound pressure radiation by assuming that the top plate is included in an infinite rigid baffle and each elementary plate surface is an equivalent point source in the rigid wall. The sound pressure amplitude is given as follows where ρ is the air density, $\tilde{Q}_i(\omega) = \tilde{V}_i(\omega)\Delta S_i$ is the source strength of i^{th} equivalent source with area ΔS_i, $k(\omega)$ is the wave number and r_i is the distance of i^{th} source to the receiving point.

$$\tilde{P}(\omega) = \frac{j\omega\rho}{2\pi}\sum_i \frac{\tilde{Q}_i(\omega)}{r_i} e^{-jk(\omega)r_i} \tag{13}$$

Compared with conventional boundary element analysis, Rayleigh integral approximates sound pressure in a fraction of the required computation time[16]. Hence, it is most suitable for parametric design studies. Although some researchers[16] have pointed out that Rayleigh integral may give large errors for sound pressure prediction if applied to strongly directional, three dimensional (3D) fields, such errors are not significant here due to the flat (rather than curved) top plate and favorable surroundings (such as rigid side plates and anechoic chamber).

B. Prediction using substitute source method

As an alternative to Rayleigh integral, a newly developed algorithm based on the substitute source approach[17] is used to compute radiated or diffracted sound field. It is conducted by removing the gearbox and introducing acoustic sources within the liberated space which yield the desired boundary conditions at the box surface (Neumann problem). Solutions are obtained in terms of the locations and/or the strengths of the substitute sources by minimizing the error function between original and estimated particle velocity normal to the interface surface[17].

Since the surface velocity distributions of gearbox are essentially symmetric along the center lines due to geometric symmetry, velocity distributions along the border lines of EFGH plane in Fig. 3(b) are chosen to simplify the 3D gearbox into a 2D radiation model for simpler data representation as well as faster computation. Zero (negligible) velocity distribution is assumed along lines EF, FG and HE since the microphone (receiver) is positioned above the center of major radiator, i.e. the top plate. A 2D line source uniformly pulsating with unit-length volume velocity Q' is chosen as the substitute source. Its radiation field is the same in any plane perpendicular to the source line. Amplitudes of the sound pressure and radial velocity of such source are given by the following, where $H_v^{(2)}$ is the Hankel function of second kind and order *v*.

$$\tilde{P}(\omega) = \frac{k(\omega)\rho c}{4}\tilde{Q}'(\omega)H_0^{(2)}[k(\omega)r], \qquad \tilde{V}_r(\omega) = -j\frac{k(\omega)}{4}\tilde{Q}'H_1^{(2)}[k(\omega)r] \tag{14a,b}$$

A "greedy search" algorithm is used to search for "optimal" substitute sources: First, a large number of candidate source positions within the vibrating body are defined, e.g. at the vertices of a square grid. Second, a single position is first found which allows the point source to produce the smallest deviation between the original and estimated normal velocity of surface vibration. The estimation is then subtracted from the original velocity to get a velocity residual. Third, among the rest of candidate points, a new position is found which makes the second source acting at it, maximally reduce the velocity residual of the first step. Once found, the source strengths of both sources are adjusted for a best fit of the original surface velocity and a new residual velocity. Each subsequent step defines a new optimum source position among the ones not already used.[17] The curve fitting of source strengths is done by minimizing the mean square root (RMS) value of the velocity error. The vector of complex source strength $\underline{\tilde{Q}}'$ is related (as shown below) to the vector $\underline{\tilde{V}}_n$ of complex normal surface velocity at control points via the source-velocity transfer matrix $\underline{\underline{\tilde{T}}}$ where $r_{ij} = \left|\vec{r}_i - \vec{r}_j\right|$ and α_{ij} is the angle between vector $\vec{r}_i - \vec{r}$ and the outer normal to the surface.

$$\underline{\tilde{Q}}'(\omega) = \underline{\underline{\tilde{T}}}^{-1}(\omega)\underline{\tilde{V}}_n(\omega), \qquad \tilde{T}_{ij}(\omega) = -j\frac{k(\omega)}{4}H_1^{(2)}[k(\omega)r_{ij}]\cos(\alpha_{ij}) \tag{15a,b}$$

To minimize the impact of an ill-conditioned matrix, the number of control points is kept well above that of independent source points. Minimization of the RMS error using pseudo-inverse yields the following, where the asterisk signifies the conjugate transpose:

$$\underline{\tilde{Q}}'(\omega) = \left[\underline{\underline{\tilde{T}}}(\omega)^*\underline{\underline{\tilde{T}}}(\omega)\right]^{-1}\underline{\underline{\tilde{T}}}(\omega)^*\underline{\tilde{V}}_n(\omega) \tag{16}$$

The difference between synthesized and original surface normal velocities is:

$$\Delta\underline{\tilde{V}}(\omega) = \underline{\underline{\Xi}}(\omega)\underline{\tilde{V}}_n(\omega), \qquad \underline{\underline{\tilde{\Xi}}}(\omega) = \underline{\underline{\tilde{T}}}(\omega)\left[\underline{\underline{\tilde{T}}}(\omega)^*\underline{\underline{\tilde{T}}}(\omega)\right]^{-1}\underline{\underline{\tilde{T}}}(\omega)^* - \underline{\underline{\tilde{I}}}(\omega) \tag{17a,b}$$

where $\underline{\underline{\tilde{I}}}(\omega)$ is the identity matrix. The matrix $\underline{\underline{\tilde{\Xi}}}(\omega)$ appears as a velocity error matrix. The RMS velocity error is normalized by dividing with the RMS value of original velocity as:

$$\tilde{e}_{RMS}(\omega) = \frac{\tilde{E}_{RMS}(\omega)}{\tilde{V}_{n,RMS}(\omega)} = \sqrt{\frac{\underline{\tilde{V}}_n(\omega)^* \tilde{\underline{\underline{\Xi}}}(\omega)^* \tilde{\underline{\underline{\Xi}}}(\omega) \underline{\tilde{V}}_n(\omega)}{\underline{\tilde{V}}_n(\omega)^* \underline{\tilde{V}}_n(\omega)}} \tag{18}$$

C. Prediction vs. noise measurements

Figure 7(a) shows predictions of surface interpolated velocity distribution on the top plate at the first three mesh harmonics under T_p = 500 lb-in and Ω_p = 4875 RPM. Note that predictions at high frequencies (e.g. mesh index m = 3) are less "reliable" due to the limitation of element dimensions as compared the wave length. The symmetry of surface velocity distribution leads to the simplification into a 2D gearbox model of Fig. 7(b). To ensure necessary accuracy for the acoustic radiation, the selected central lines of the 2D plane should capture the dominant structural modes of Fig. 7(a). Also, the structural wavelength along the central line should be higher than the acoustic wavelength of interest to ensure the validity of the 2D approach.

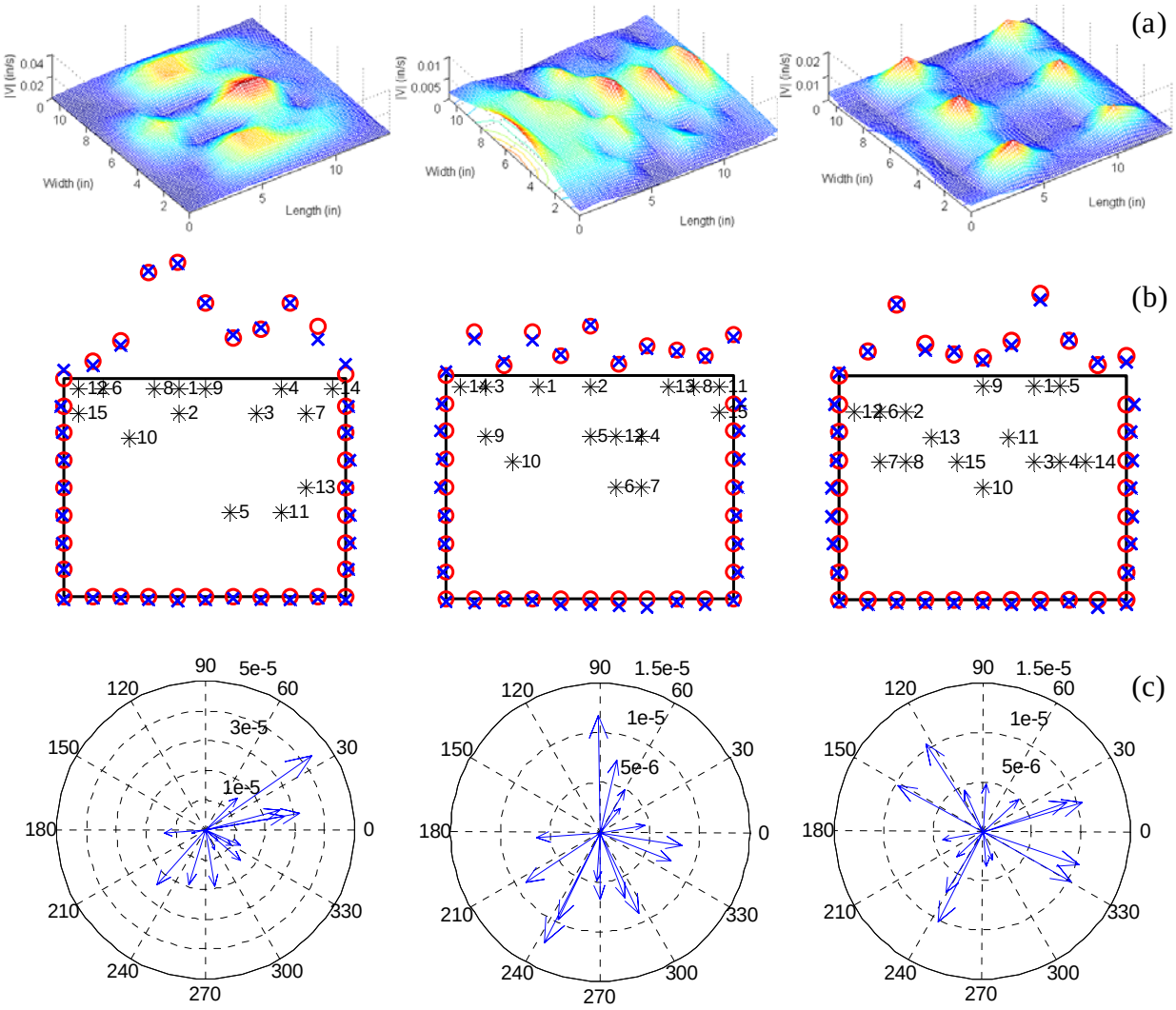

Figure 7: Comparison of normal surface velocity magnitudes and substitute source strength vectors under T_p = 500 lb-in and Ω_p = 4875 RPM. (a) Line 1: interpolated surface velocity on top plate; (b) Line 2: simplified 2D gearbox model with 15 substitute source points; Key: O, original surface velocity magnitude; ×, surface velocity magnitude by substitute sources; ✳, locations of substitute sources. (c) Line 3: substitute source strengths in complex plane for 2D gearbox. Column 1: mesh frequency index m = 1; Column 2: m = 2; Column 3: m = 3.

The source points of Fig. 7(b) are chosen from a mesh grid of candidate points not too close to the boundary to prevent forming steep gradients of surface pressure. Observe that only 15 substitute sources tend to predict well the surface distribution of velocity magnitude at the gear mesh harmonics. Figure 7(c) illustrates the predicted source strengths of the substitute sources in the complex plane for evaluation of the acoustic source properties. A single dominant substitute source is observed at the first mesh harmonic (monopole-like acoustic source); however, several dominant substitute sources are present and these are more equally distributed in the complex plane at the higher harmonics (multi-pole acoustic source). The simplification from 3D into 2D gearbox model requires examining surface modes and a careful selection of representative plane, which poses additional limitations to its application as a universal method. However, once applicable, the substitute source method provides the following benefits. First, it enables an efficient evaluation of the acoustic source characteristics for whine noise. Second, unlike the Rayleigh integral which assumes that the top plate is part of an infinite rigid baffle, it takes the body shape into account and thus reduces the errors especially in the low frequency range. This also allows a straight forward synthesis of the radiation field for all the sources by using simple superposition as diffraction on the sources does not take place. Finally, compared with boundary element analysis, it does not suffer from the problems of singularities or uniqueness of solution. Nonetheless, it is an approximate method.

Figure 8 compares sound pressure measured at the microphone 6 inch above the top plate to predictions by using both the Rayleigh integral as well as the substitute source method under varying pinion torque given Ω_p = 4875 RPM and 140 °F. Predictions correlate well with measurements in terms of trends and relative magnitudes at first three gear mesh harmonics.

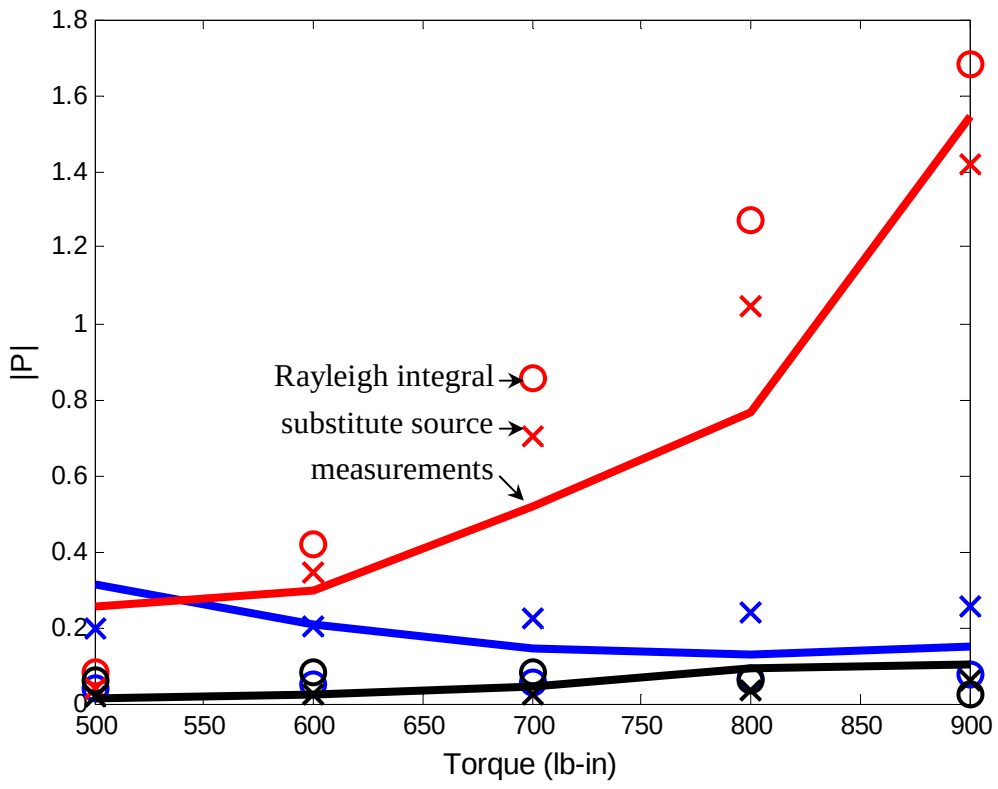

Figure 8: Normalized sound pressure (re 1.0 Pa) predicted at the microphone 6 inch above the top plate under varying torque T_p given Ω_p = 4875 RPM and 140 °F. Key: ——, measurements; ○, Rayleigh integral predictions ×, substitute source predictions. Blue, mesh frequency index m = 1; red, m = 2; black, m = 3.

5. CONCLUSIONS

A refined source-path-receiver model has been developed which characterizes the sliding friction induced structural path and associated noise radiation. Proposed Rayleigh integral method and substitute source technique are more efficient for calculating the acoustic field than the usual boundary element technique and thus they provide rapid design tools to quantify the frictional noise. Figure 9 compares the sound pressure level predicted given Ω_p = 4875 RPM and 140 °F under T_p = 500 lb-in (close to the "optimal" load where transmission error is minimized) and under high torque with T_p = 800 lb-in. At each gear mesh frequency, individual contributions of transmission error (via the LOA path) and frictional effects (via the OLOA path) are compared to the overall whine noise. Observe in Fig. 9(a) that near the "optimal" load, friction induced noise is comparable to the transmission error induced noise (especially for the first two mesh harmonics); thus sliding friction should be considered as a significant contributor to whine noise. However, at non-optimal torques in Fig. 9(b), friction induced noise is overwhelmed by the transmission error noise, thus sliding friction could be negligible under such conditions. Further work is needed to fully examine the friction source, especially under varying lubrication conditions. Effects of the tooth surface finish should be examined as well.

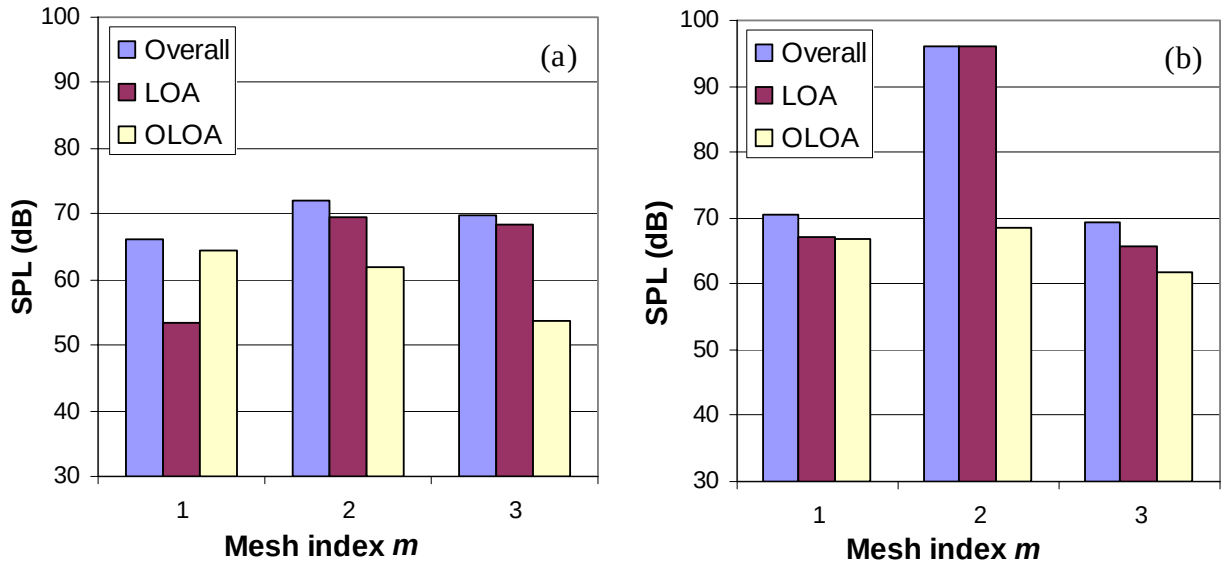

Figure 9: Overall sound pressure levels (ref: 2e-5 Pa) and their contributions predicted at the microphone 6 in above the top plate under Ω_p = 4875 RPM and 140 °F. (a) T_p = 500 lb-in (optimal load for minimum transmission error); (b) T_p = 800 lb-in.

ACKNOWLEDGEMENTS

We gratefully acknowledge the Marie Curie Fellowship of the European Commission for financially supporting this research. V. Asnani and F. Oswald of the NASA Glenn Research Center are thanked for conducting the experiments. We acknowledge Dr. T. Rook of Goodrich Co. and Dr. R. Gunda of Advanced Numerical Solutions Inc. for their comments and suggestions. Dr. T. Lim from the University of Cincinnati is thanked for providing the bearing stiffness software.

REFERENCES

[1] D. R. Houser, "Comparison of transmission error predictions with noise measurements for several spur and helical gears," *NASA-Technical Memorandum*, 106647, *30th AIAA Joint Propulsion Conf.*, Indianapolis, IN, (1994).

[2] G. Steyer, "Influence of gear train dynamics on gear noise," *NOISE-CON* 87 *Proc.*, 53-58 (1987).

[3] M. Ajmi, and P. Velex, "A model for simulating the quasi-static and dynamic behavior of solid wide-faced spur and helical gears," *Mech. Machine Theory*, **40**, 73-190 (2005).
[4] P. Velex and V. Cahouet, "Experimental and numerical investigations on the influence of tooth friction in spur and helical gear dynamics, *ASME J. Mech. Design* **122** (4), 515-522 (2000).
[5] O. Lundvall, N. Strömberg and A. Klarbring, "A flexible multi-body approach for frictional contact in spur gears," *J. Sound Vib.*, **278**(3), 479-499 (2004).
[6] S. He, R. Gunda and R. Singh, "Effect of sliding friction on the dynamics of spur gear pair with realistic time-varying stiffness," *J. Sound Vib.*, **301**, 927-949 (2007).
[7] External2D (CALYX software), A contact mechanics/finite element (CM/FE) tool for spur gear design, ANSOL Inc., Hilliard, OH.
[8] T. C. Lim and R. Singh, "Vibration transmission through rolling element bearings. Part I: bearing stiffness formulation," *J. Sound Vib.*, **139**(2), 179-199 (1990).
[9] T. E. Rook and R. Singh, "Mobility analysis of structure-borne noise power flow through bearings in gearbox-like structures," *Noise Control Eng. J.*, **44**(2), 69-78 (1996).
[10] A. Van Roosmalen, "Design tools for low noise gear transmissions," Ph. D. Dissertation, Eindhoven University of Technology (1994).
[11] T. E. Rook and R. Singh, "Structural intensity calculations for compliant plate-beam structures connected by bearings," *J. Sound Vib.*, **211**(3), 365-388 (1998).
[12] F. B. Oswald, A. F. Seybert, T. W. Wu and W. Atherton, "Comparison of analysis and experiment for gearbox noise," NASA-TM-105330 (1992).
[13] R. Singh, "Dynamic analysis of sliding friction in rotorcraft geared systems," technical report submitted to the Army Research Office, grant number DAAD19-02-1-0334 (2005).
[14] M. F. Jacobson, R. Singh and F. B. Oswald, "Acoustic radiation efficiency models of a simple gearbox," NASA Technical Memorandum 107226 (1996).
[15] L. Cremer and M. Heckl, "Structure-borne sound," Chap. 6 in *Sound Radiation from Structures*, (Springer-Verlag, New York, 1973).
[16] D. W. Herrin, F. Martinus, T. W. Wu and A. F. Seybert, "A new Look at the high frequency boundary element and Rayleigh integral approximations," *SAE*, paper # 03NVC-114 (2003).
[17] G. Pavic, "An engineering technique for the computation of sound radiation by vibrating bodies using substitute sources," *J. Acta Acustica*, **91**, 1-16 (2005).